The effect of modified tannic acid (TA) eco-epoxy adhesives on mode I fracture toughness of bonded joints

Mohamed Nasr Saleh [a],[*],[1], Nataša Z. Tomić [b],[1], Aleksandar Marinković [c], Sofia Teixeira de Freitas [a]

[a] Structural Integrity & Composites Group, Faculty of Aerospace Engineering, Delft University of Technology, the Netherlands
[b] Innovation Center of Faculty of Technology and Metallurgy in Belgrade Ltd, Karnegijeva 4, Belgrade, Serbia
[c] Faculty of Technology and Metallurgy, University of Belgrade, Karnegijeva 4, 11070, Belgrade, Serbia

ARTICLE INFO

ABSTRACT

Two synthesized eco-epoxy components based on TA: (A) glycidyl ether and (B) glycidyl phosphate ester, are used, as a replacement for the Bisphenol A (BPA) based epoxy component, for bonding aluminum (Al) and carbon fiber reinforced polymer (CFRP). Their effect on the mode I fracture toughness (G_I) is evaluated by Double Cantilever Beam (DCB) testing while using Digital Image Correlation (DIC) for in-situ crack tip monitoring. Compared to the reference adhesive, an improvement of (G_I) of Al (43%) and CFRP (100%) is obtained when using adhesive B. Moreover, regardless of the adherend material, a stick-slip pattern of crack growth is observed. Weak adhesion of the reference adhesive leads to an adhesive failure vs. a cohesive-adhesive failure in the case of adhesive B. On the contrary, the modification of adhesive A has an adverse effect on the G_I of Al (−33%) and CFRP (−78%) as opposed to their reference counterparts.

1. Introduction

The growing consumption of polymeric materials led to higher environmental and economic concerns, which in return resulted in encouraging more research and development activities of bio-based monomers and replacement of petroleum derivatives [1]. The production of bio-based materials from bio-renewable sources ensures lower toxicity and protection of the environment as well as better recyclability and sustainability [2]. Most of the natural products have gained high interest due to their specific chemical structures that can be utilized in the production of new building blocks, and thus helping the bio-based industry (BBI) to grow [3]. Bisphenol A (BPA) is one of those controversial petroleum based chemicals which is widely used in polymer industry. Although it is found to be carcinogen, reprotoxic [4], and thus banned for the usage in baby's products such as bottles [5], it is still used in health and food related products due to the excellent properties that BPA provides. The majority of BPA (90%) in the chemical industry accounts for the production of epoxy resins and polycarbonates [6]. Nowadays, approximately 75% of commercial epoxy resins are synthesized via the reaction of BPA and epichlorohydrin, producing resin called diglycidyl ether of bisphenol A (DGEBA).

Significant research efforts have been made to replace the BPA component with natural resources such as vegetable oils [7], lignin [8], tannin [9], sugar [10], cardanol [11], isosorbide [12] and itaconic acid [13]. Bio-based resources such as lignin, tannin and cellulose possess numerous hydroxyl groups in their structure, which are highly favorable in establishing good adhesion properties on various substrates [14–16]. Besides their good adhesive properties, their phenolic groups contribute to high thermal stability and fire resistance properties. The reactive hydroxyl groups are easily converted into epoxy functionalities that can create bio-based epoxy polymer network [17–19]. Tannins are employed in the production of formaldehyde wood adhesives since 1970s [20]. Nowadays, they are attracting more attention in the synthesis of prepolymers for bio-based epoxy resins and adhesives [21–24]. Novel synthetic routes are proven to be a promising strategy for the aforementioned prepolymers as the obtained materials showed comparable or even better properties than their commercial counterparts [25]. Tannic acid (TA) is the most commonly functionalized group in the reaction of epichlorohydrin to obtain glycidyl ether derivative [21,26]. The introduction of carboxylic groups to TA is used as a modifier for the

---

epoxy/anhydride curing systems [27]. The introduction of phosphorous content in TA was done via triethyl phosphate to improve the adhesion of Teflon to metals and obtain high thermal stability [28]. In other words, the introduction of epoxy functionalities with the phosphoryl group linkage should provide an improved adhesion, higher reactivity and thermal stability. So far, TA based adhesives are commonly tested for wood application thanks to their good compatibility. Nevertheless, characterization of TA based adhesives for other adherends has not been investigated or reported in the open literature. Only one recent study, by the authors, showed that the modified TA can establish an enhanced interface adhesion on aluminum (Al) and carbon fiber reinforced polymer (CFRP) as opposed to commercial DGEBA [29] using the bell peel test (BPT). Thus, the objective of this study is to focus and dedicate more attention to the characterization of TA based adhesives for adherends used in light-weight applications such as Al and CFRP.

Epoxy adhesives are generally brittle materials, and any changes in their chemical formulation could significantly affect their mechanical properties and their damage tolerance [30]. Fracture toughness is one of the most important properties of any adhesively bonded joint, reflecting its resistance to crack propagation, either in the bulk adhesive or at the adhesive-adherend interface. Despite the wide use of epoxy adhesives in structural and non-structural applications, their brittle nature causes great losses of the structural integrity when damage occurs. Therefore as a first attempt to investigate the advantages that such novel eco-epoxy based adhesives can offer, the mode I fracture toughness using Double Cantilever Beam (DCB) testing [31–33] is chosen to be the focus of this study with more interfacial shear characterization to follow in future studies. From the materials point of view, two components based on modified TA: (A) glycidyl ether and (B) glycidyl phosphate ester of TA, are synthesized and proposed as a bio-based replacement of the BPA based epoxy component. In addition, their adhesion is analyzed on two different substrates: Al and CFRP, which are commonly used for light-weight structures. The DCB test is carried out by applying a normal displacement to the crack plane with an initial pre-cracking length (a_0). Crack length is then monitored during the test and correlated to the load and displacement values to calculate the initiation and propagation fracture toughness. Fabrication of DCB specimens is straightforward and testing can be easily implemented by a standard testing machine. That is why this test method is chosen for evaluating the performance of the newly synthesized eco-epoxy based adhesives. However, it is worth mentioning clearly that improving the interfacial strength between the adhesive and adherend via some of the widely used techniques, such as surface treatments, is out of the scope of this study. The objective of this research work is only to compare the performance of the two synthesized eco-epoxy based adhesives against a reference commercially used DGEBA adhesive, and understand the effect of such modifications on the fracture toughness and failure mechanism.

This paper includes five more sections. Section 2 describes the materials used, the synthesis procedure of the adhesives and the manufacturing process of the bonded joints. This is then followed by the experimental procedure discussion in section 3. Detailed description of the data reduction techniques and theory of the mode I DCB fracture toughness is depicted in section 4. Afterwards, section 5 details the main experimental findings of the study with a thorough scientific discussion. Finally, a reflection and summary of the key conclusions is summarized in section 6.

2. Materials and manufacturing

2.1. Adhesives and adherends

Chemicals used in synthesis of the modified TA are epichlorohydrin (EPH), sodium hydroxide (NaOH), deionized water (MiliQ), chloroform, acetone N-methyl-2-pyrrolidone (NMP), Tetrahydrofuran (THF), phosphorus oxychloride (POCl$_3$), glycidol, magnesium sulphate and calcium chloride. All the chemicals were supplied from Sigma-Aldrich Chemie

Gmbh, Steinheim, Germany, and used as received. The selected reference adhesive was diglycidyl ether of bisphenol A (DGEBA – LG700 epoxy component and HG 700R curing agent – isophorone diamine) supplied by GI-NI ltd, Belgrade, Serbia (epoxy value 0.62, T_g = 79.4 °C).

Two types of adherends were selected: Al alloy 2024 and CFRP composites HexPly 8552 unidirectional prepreg epoxy resin in combination with AS4 carbon fiber (Hexcel Composites, Cambridge, UK). CFRP laminates were manufactured in the autoclave with a curing cycle of 180 °C for 120 min at 7 bars of pressure.

2.1.1. Modification of TA

2.1.1.1. Synthesis of glycidyl ether of TA.
Glycidyl ether of TA was synthesized via the reaction of TA and EPH at 80 °C, with 1:1.5 wt ratio of TA to NaOH [24]. Dissolved EPH (15 g) in 15 ml of THF was placed in a three-neck round-bottomed flask with a reflux condenser, dropping funnel at room temperature and under nitrogen atmosphere. TA (3 g) was then added to the solution of EPH and heated up to 80 °C under constant magnetic stirring. Once the temperature was reached, 20% NaOH water solution (22.5 ml) was added using a dropping funnel. After 3 h at 80 °C, the mixture was left to cool down, and then 200 ml of cold MiliQ water was added slowly. The product was extracted with toluene and dried with MgSO$_4$ overnight. The toluene solution was filtrated and distilled under vacuum (~1 kPa). The obtained product was a highly viscous brownish liquid. The measured epoxy equivalent weight was EEW = 170 g/mol, which means that 10 epoxy groups per one TA molecule were introduced. The chemical structure was characterized and detailed in the previously published work [29].

2.1.1.2. Synthesis of glycidyl phosphate ester of TA.
Glycidyl phosphate ester of TA was synthesized according to a novel procedure inspired by the fire resistant epoxy derivatives of TA [34]. Dissolved TA (6 g) in 50 ml of chloroform/NMP (1:1) mixture was placed in a 250 ml three-neck round-bottomed flask. The vacuum distillation apparatus was set up together with two pressure equalizing dropping funnels. After 30 min of mixing, the temperature was increased up to 70 °C. One dropping funnel was filled with a solution of 9.75 g of POCl$_3$ in 20 ml of chloroform, and the second one with 9.42 g of glycidol dissolved in 40 ml of chloroform. These solutions from the funnels were added dropwise under constant stirring and a low vacuum (~1 kPa). The POCl$_3$ solution was added for 1 min and then, after 10 min, the glycidol was added during the next 2 min. Following the same protocol, the addition continued until the whole amount of reactants were added. Afterwards, the temperature was increased up to 85 °C and the vacuum was gradually increased, until all the chloroform was removed. The reaction lasted for 12 h, and then the vacuum was increased (10 Pa) to remove the NMP. The product was purified analogously to the glycidyl ether of TA. The obtained product was a highly viscous brown liquid. The measured epoxy equivalent weight was EEW = 85 g/mol, which means that 20 epoxy groups per one TA molecule were introduced via 10 phosphoryl linkages. Similarly, the reader is referred to Ref. [29] for the detailed chemical characterization of the structure. In this study, only the chemical structure of both types of adhesive components, obtained by the modification of TA, is presented in Fig. 1.

2.2. Surface pretreatments and bonding

Prior to bonding, the surface preparation of aluminum samples was as follows: I- acetone cleaning, II- grit blasting with Al$_2$O$_3$ powder (Corublast Super Z-EW No. 40, Ø 0.35–0.50 mm), III- acetone cleaning and IV- air blow duster gun. For the CFRP, the surface was prepared in steps as follows: I- acetone cleaning, II- sanding (240 grit size) in ±45° direction, III- acetone cleaning, IV- air blow duster gun and V- UV/ozone treatment (7 min of exposure). The UV/ozone apparatus, used for surface treatment of CFRP samples, consisted of three UV lamps (30 W, λ =
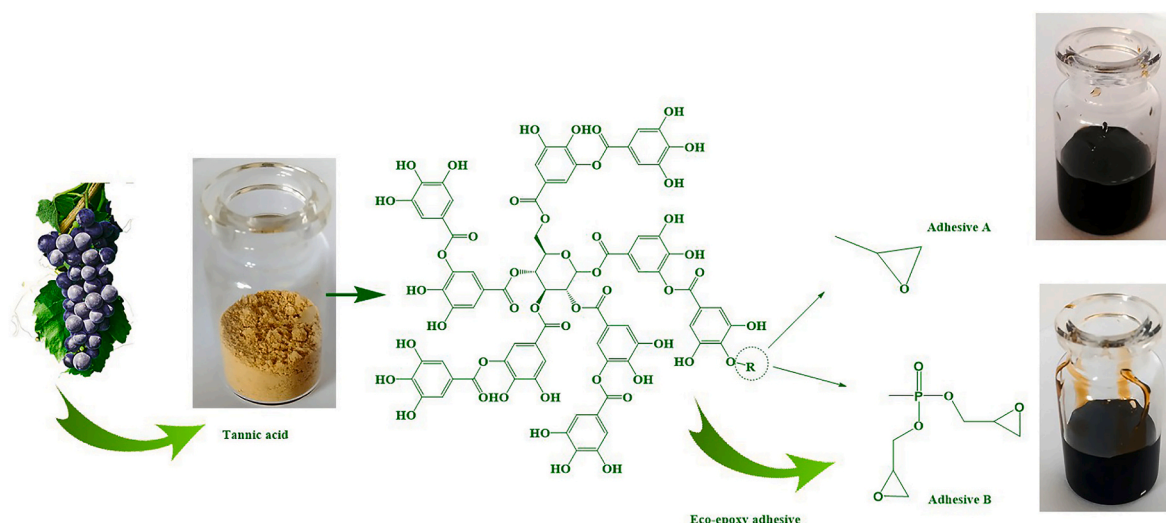
Fig. 1. The chemical structure of the modified tannic acid and the process to obtain the eco-epoxy components.

184.9 nm and 253.7 nm) with a sleeve of natural Quartz (UV-Technik, Wümbach, Germany) at atmospheric conditions. UV/ozone treatment is easy precision dry cleaning method in a wide range using high intensity UV light in ozone atmosphere (generated from environmental air) [35].

Three adhesives were selected for testing the adhesion on both adherends: 1) reference epoxy adhesive (REF); 2) epoxy adhesive with 15 wt% of glycidyl ether of TA (type A adhesive); and 3) epoxy adhesive with 15 wt% of glycidyl phosphate ester of TA (type B adhesive). The effect of eco-epoxy components on the interface adhesion was estimated by the adhesion parameter *b*, which was compared to the reference epoxy (REF). Adhesion parameter *b* showed that the interface adhesion is significantly enhanced by the addition of both A and B eco-epoxy components [29]. The replacement of TA component more than 15 wt % deteriorate the processibility and the applicability of the adhesives. Thus, the content of 15 wt% was selected for further characterization. Glass bead spacers, used for adhesion thickness control, were mixed with the adhesives at 0.1 wt% prior to bonding. Bonding of materials was performed at room temperature for 24 h, with post-curing on 70 °C for 4 h according to the producer's specification. The measured final adhesive thickness was 200 ± 20 μm. After curing, the samples were cut to 25 mm wide rectangular specimens using a precision water-cooled diamond wheel.

Afterwards, the loading blocks were bonded to the CFRP DCB specimens using a two-component Scotch-Weld Structural Epoxy Adhesive 9323 B/A from 3 M Ltd. The bonding adhesive had a mixing ratio of 100/27 by weight. The adhesive was cured for 24 h at room temperature and then post-cured for 2 h at 65 °C as per the manufacturer guidelines.

For the Al DCB specimens, drilled holes were threaded in the un-bonded sections of both arms and the loading blocks were directly attached by screws to each side.

3. Experimental procedure

3.1. DCB testing

The mode I fracture toughness DCB test was carried out, according to the ISO 25217 standard [36], using displacement-controlled mode (3 mm/min). The machine used for testing was a Zwick Roell machine equipped with a 10 kN load cell and hydraulic grips to minimize the slippage due to gripping. Both the crosshead displacement and the applied force were recorded by the machine during the test. The test setup is depicted in Fig. 2a. Five repeats of each adhesive type for both Al and CFRP were tested. All the specimens had the same nominal dimensions (length x width ~ 250 mm × 25 mm) with a 70 mm long Teflon sheet to act as the crack initiator (see Fig. 2b). All specimens were designed so that the distance between the loading pin and the initial crack tip is ~50 mm as per the ISO 25217 standard procedure. The only difference was the adherends thickness being 6 mm and 2.4 mm for Al and CFRP respectively. For each material and each adhesive type, five specimens were tested to ensure the reproducibility and repeatability of the results.

As per the standard recommendations [36], the test was carried out on two steps: i) Initial loading and ii) Reloading. The objective of the initial loading step is to create a sharp crack tip by allowing the initial
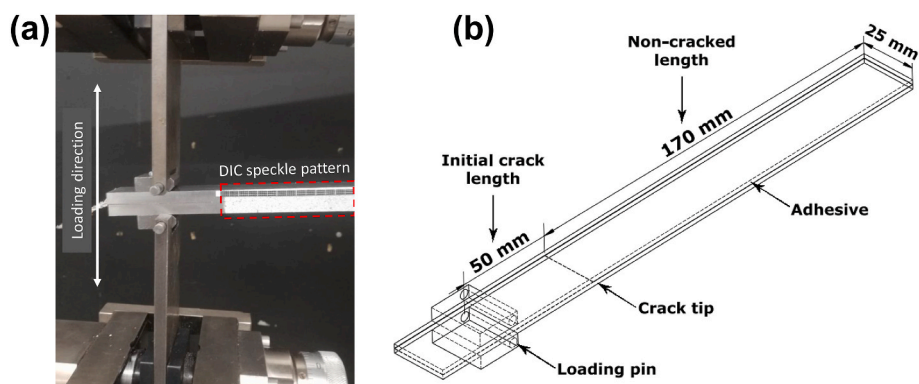

Fig. 2. a) DCB test setup and b) schematic of the DCB specimen.

debonding to propagate for few millimeters at a constant crosshead displacement rate. After unloading, the specimen was again reloaded at the same constant crosshead speed as the initial loading, but this time without stopping the test till the final failure was reached.

3.2. Digital Image Correlation (DIC)

In order to visualize the full field displacement contour map ahead of the crack tip [37,38] and measure the crack length throughout the test [39,40], two-dimensional (2D) DIC system (see Fig. 2a) was used. The DIC system consisted of a 8-bit "Point Grey" camera with a resolution of 5 MP, equipped with a "XENOPLAN 1.4/23" lens. The software used for capturing and recording the speckle pattern images was ViC-Snap 8, a product of "Correlated Solutions Inc.". The observation window of approximately (650×650) mm^2 produced an image with dimensions of (2048×2048) pixels. The acquisition rate of 1 and 0.33 frames per second (fps) was used for the initial and reloading tests respectively. Analogue outputs from the testing machine were used to synchronize saving the acquired images with their corresponding load and displacement at each point in time. This is very essential when it comes to calculating the fracture toughness as function of the load, displacement and crack length. Afterwards, the acquired images by ViC-Snap 8 were processed using ViC-2D 6 software.

3.3. Fractured surface analysis

The post-mortem fractured surfaces of representative specimens from each tested group are analyzed in order to determine the type of failure using 3D optical microscope with a wide-area 3D measurement system, VR-5200 from Keyence, Itasca, Illinois, USA. The scanner is characterized by < 100 nm out-of-plane resolution with up to a 206×104 mm^2 measuring area.

4. DCB analysis and data reduction techniques

This section is intended to discuss the data reduction techniques in the light of the ISO 25217 and explain the reasons for the selected approach in this study. An illustrative example for the load-displacement curve for mode I DCB test is depicted in Fig. 3a. At a constant crosshead displacement rate, the curve is characterized by a linear segment in the beginning after which a deviation from linearity occurs, and it continues increasing up to a maximum/peak load. Once this peak load is reached, a softening region is observed, in which the load decreases as a function of the applied displacement. As shown in Fig. 3 a, there exists several values on the load-displacement curve that can be used for the determination of the mode I initiation fracture toughness (G_{Ic}). These points represent the onset of the crack propagation and they are conventionally referred to as: i) Deviation form linearity (NL), ii) Visual observation (VIS) and 5% offset. The NL approach assumes that the crack starts to grow from the middle of the specimen

before being observed by visual inspection at the edges. In the case of brittle adhesive, this NL value should be very close to the VIS value. However, for ductile/tough adhesives there is a chance to have a nonlinear region in the load displacement curve preceding the visual observation of the crack at the edges. Thus, the NL calculated value always represents a conservative lower bound for G_{Ic} (see Fig. 3b). The third value can be determined as the intersection between the load-displacement curve and an offset line drawn from the origin which has a 5% increase in the compliance as opposed to the linear segment of the curve.

For both the initiation and propagation G_{Ic} calculations, there exist three data reduction techniques as per the ISO 25217. These methods are: i) the simple beam theory (SBT), ii) the corrected beam theory (CBT) and iii) the experimental compliance method (ECM). The reader is referred to the standards for detailed discussion and derivations. The SBT theory calculates the strain energy release rate G_I assuming there is no rotation at the delamination/crack front, as follows:

$$G_I = \frac{4P^2}{E_s b^2}.m \tag{1}$$

$$m = \frac{3a^2}{h^3} + \frac{1}{h} \tag{2}$$

where:

P = applied load,
E_s = the adherend flexure modulus,
b = the specimen width, and
a = the delamination length, and
h = the adherend thickness

In practice, this assumption overestimates the values of G_I because the DCB is not perfectly clamped (built-in). In order to account for this rotation, the DCB specimen is assumed to have a longer crack/delamination length $a + |\Delta|$, where $|\Delta|$ can be determined from a graph of the cubic root of the compliance, $C^{1/3}$, as a function of the delamination length. The intersection of the least squares fit with the x-axis is $|\Delta|$, and the compliance, C, is the displacement-to-load ratio, δ/P, and the corresponding points are determined as function of the visually observed delamination length starting from the onset point. The mode I fracture toughness, calculated using the CBT, is thus determined as:

$$G_I = \frac{3P\delta}{2b(a+|\Delta|)}.\frac{F}{N} \tag{3}$$

$$F = 1 - \frac{3}{10}\left(\frac{\delta}{a^2}\right)^2 - \frac{3}{2}\left(\frac{l_1\delta}{a^2}\right) \tag{4}$$

$$N = 1 - \left(\frac{l_2}{a}\right)^3 - \frac{9}{8}\left[1 - \left(\frac{l_2}{a}\right)^2\right]\left(\frac{l_1\delta}{a^2}\right) - \frac{9}{35}\left(\frac{\delta}{a}\right)^2 \tag{5}$$
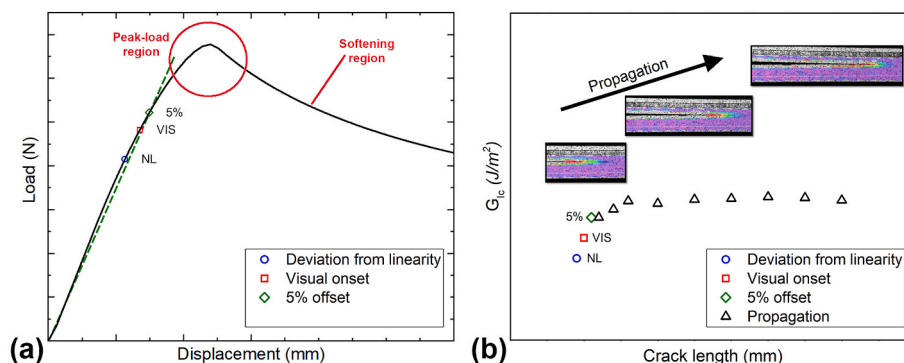

Fig. 3. A schematic representation of a mode I DCB test results: a) Load-displacement curve and b) Delamination Resistance Curve (R-curve).

where:

l_1 = the distance from the center of the loading pin to the mid-plane of the arm to which the loading block is attached, and
l_2 = the distance from the center of the loading pin to the edge of the block

The ECM requires the logarithm of the compliance, $\log(C)$, to be plotted against the logarithm of the crack length, $\log(a)$. The slope (n) is then used for G_I calculation as follows:

$$G_I = \frac{nP\delta}{2ba} \cdot \frac{F}{N} \tag{6}$$

Out of all the three proposed techniques, the CBT leads to the most conservative G_I values [36,41]. Thus, this data reduction method is the one chosen for the rest of the discussion in this study.

The delamination/crack propagation during the DCB test results in a typical resistance-type fracture behavior (see Fig. 3b) in which G_I increases linearly and then stabilize with further crack growth. The behavior is referred to as the resistance curve (R-curve). As far as this study is concerned, the visual observations using the DIC are used to determine the G_I propagation values as detailed in section 5.3.

5. Results and discussion

5.1. Crack tip monitoring using DIC

DIC was successfully used by Murray et al. [40] to accurately monitor the crack tip during interlaminar mode I and mode II fracture testing under both static and fatigue loading conditions. They recommended using the confidence in pixel correlation, "sigma", to define the crack front position throughout the test. The same DIC system, used in this previous study, was utilized in the current study. To be able to monitor the crack tip position during the testing, a threshold value of sigma should be defined. This threshold value (0.01 pixel) would then be used to indicate the location of the crack front throughout the whole testing. In order to evaluate the dependency of the crack tip location on the post-processing parameters, they carried out a parametric study by varying the size of: i) the subset and ii) the step (see Fig. 4a). The subset size (S_i where $i = 0,1,...,n$) is the smallest unit of area that is used to track the displacement, and its size should be large enough to contain a

sufficiently distinctive pattern for correlation. The step size (S_s) controls the spacing between the points analyzed during the processing of the region of interest (ROI). They concluded that the smaller the step size, the higher the overlap and loss of independent information of the individual subset measurements. Thus as best practice guidelines, the step size of at least 0.25–0.33 of the subset size should be used. Using the recommendations from Murray et al. [40], the step size of (10 and 8) and subset size of (35 and 29) were used in this analysis for the crack tip monitoring using the DIC for the Al (see Fig. 4b) and CFRP (see Fig. 4c) cases respectively.

One advantage of using DIC is the ability to monitor the adherends' vertical displacements (v) throughout the DCB testing. In reality, the deformation of the adhesive layer ahead of the crack tip results in some vertical displacement of the adherends within the bonded zone. This translates into a non-zero displacement at the crack tip. This is a well-established understanding, previously detailed in the open literature [42]. The concept is to segment the DCB adherends, along their length, into two regions as shown in the schematic in Fig. 5: i) unbonded and ii) bonded, based on the Euler–Bernoulli beam theory and the Winkler elastic foundation [43]. In the unbonded segment, both adherends can be treated as two cantilever beams moving symmetrically apart from the mid-plane of the bond-line. However, the second region is the bonded region including the process zone ahead of the crack tip. The length of the zone, over which the positive peel stress is distributed, is designated by (λ^{-1}) which is dedicated by the geometry and material properties of both the adhesive and adherends [42]. The parameter λ is defined as $\lambda = \sqrt[4]{k/4EI}$, where k is the stiffness of the elastic foundation ($k = bE_{ad}/t$) for the plain strain case. E is the adherend's stiffness, I is the second moment of area, b and t are the adherend's width and half thickness, respectively and E_{ad} is the adhesive's stiffness. The reader is referred to Ref. [42] for the detailed derivation.

In the light of the previous discussion and to investigate the validity of the proposed DIC crack tip monitoring approach, Fig. 5 depicts the vertical displacement (v), measured by DIC, along a line in the top adherend for one representative specimen of Al (see Fig. 5a) and CFRP (see Fig. 5b). The behavior was repeatable and reproducible for all the tested specimens regardless of their adherend material. Five plots are presented corresponding to the crack propagation in the form of five different crack lengths "a_0 to a_4" during the test, with a_0 representing the reference/initial case. Moreover, the crack tip location, calculated by the sigma approach from the DIC, is marked on each plot (see
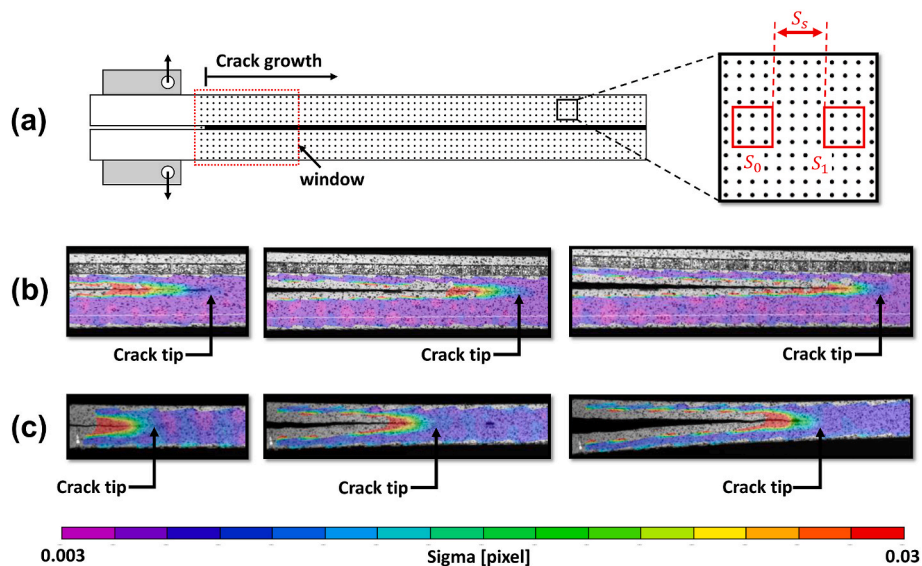

Fig. 4. a) A schematic of the DCB specimen defining the DIC subset and step parameters, Crack tip front monitoring using the confidence in pixel correlation "sigma" using the moving window highlighted in the schematic, for b) Al and c) CFRP.
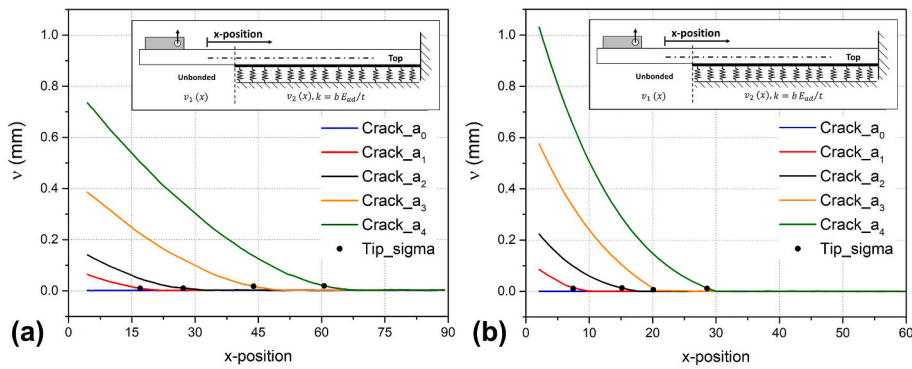
Fig. 5. A representative vertical displacement (v) curve, obtained from the DIC analysis and used for the crack tip monitoring, along the top adherend during DCB test as a function of the x-position: a) Al and b) CFRP.

"Tip_sigma" in Fig. 5a and b). It is clear from Fig. 5 that the vertical displacement (v) corresponding to the different crack lengths is not equal to zero, for both Al and CFRP cases. This goes in a good agreement with the aforementioned theory which is based on Euler–Bernoulli beam theory and the Winkler elastic foundation. Thus, all the analysis for the DCB and the fracture toughness calculations in sections 5.2 and 5.3 is based on the crack tip monitoring using the proposed DIC approach explained in this section.

5.2. DCB analysis

One representative load-displacement curve, for each adhesive type for the Al and CFRP adherends, is depicted in Fig. 6a and Fig. 7a respectively. In both cases, it is clear that adhesive A has the highest compliance amongst all adhesive types. This can be directly explained in the light of the initial loading step, which was carried out to create the sharp crack front. The initial loading for adhesive A for Al and CFRP led to a longer initial crack/delamination (~75–80 mm), thus affecting the compliance of reloading curves. On the contrary for the reference and adhesive B, the initial crack length after the initial loading stage was comparable (~55–60 mm), and consequently their compliance in both Al and CFRP cases is similar. To eliminate the compliance effect, the displacement and load can be normalized to non-dimensional quantities (N_D and N_L) respectively. The normalized displacement is defined as ($N_D = d/a_0$), where d is the applied displacement and a_0 is the crack length after the initial loading. The normalized load is defined as ($N_L = Fa_0^2/EI$), where F is the applied load, E is the adherend's stiffness and I is the second moment of area. The normalized curves for Al and CFRP cases are shown in the top right corners of Figs. 6a and 7a respectively. For the Al adherends, the maximum/peak load is the highest for adhesive B (~190 N) followed by the reference (~150 N) and the least is

adhesive A (~105 N). The same observation applies for the displacement (adhesive B > reference > adhesive A).

In addition, the load-displacement pattern of adhesive B differs from the other two. Both reference and adhesive A response follows the typical DCB load-displacement, as previously introduced in section 4, with a linear segment in the beginning up to the peak load, then softening region. This suggests a stable continuous crack growth pattern. On the contrary for adhesive B, the load-displacement curve demonstrates the classical well-known phenomenon of stick-slip for mode I DCB testing [44,45]. Blackman defined the stick-slip feature as the discontinuous non-steady crack growth which is captured experimentally in the form of a series of rapid bursts (slip), interspaced by periods of crack arrest (stick) [44]. The concept is analogues to the static vs. kinetic coefficient of frictions in the sense that there exists a competition between the resistance of a crack to initiation versus its resistance to continued propagation. According to the ISO 25217 [36], the reasons for such phenomenon is not yet fully understood. However, Heide-Jørgensen et al. [45] provided one possible interpretation of this stick-slip phenomenon is the light of the crack locus shift from the cohesive, inside the strongly adhering bond-line zone, to the interfacial, along the adherend/adhesive interface. This is thought to be the main reason for this stick-slip pattern in the case of adhesive B with the Al adherends as it will be later detailed using the fractured surfaces (see Fig. 10c and 11e). One of the main consequences of the stick-slip behavior is that a series of initiation and arrest points can be identified in the load-displacement curves as well as sudden propagations in the recorded crack length can be observed (see. Fig. 6b). The change of the crack length ($\Delta a = a_i - a_0$) is plotted versus the crosshead displacement in Fig. 6b to determine the crack propagation/growth rate. The crack propagation rate is defined as the slope of the least squares fit of the change of the crack length (Δa) as a function of the crosshead
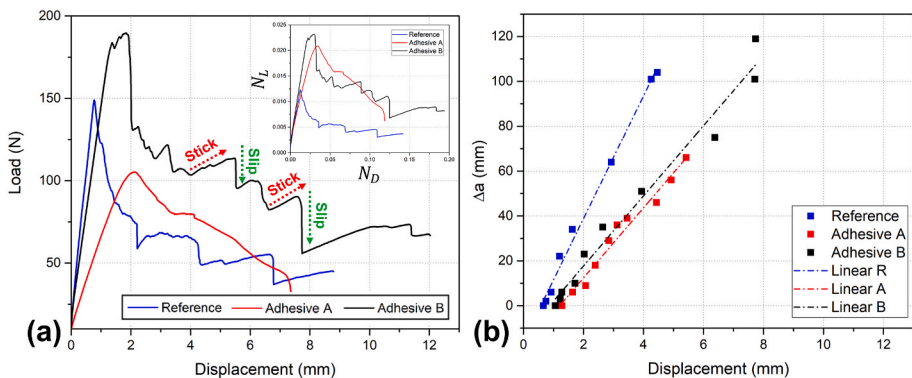

Fig. 6. Representative response of the Al DCB specimens: a) reloading load-displacement curves "top right corner for the normalized N_L vs. N_D curves" and b) Crack length propagation as a function of the crosshead displacement.
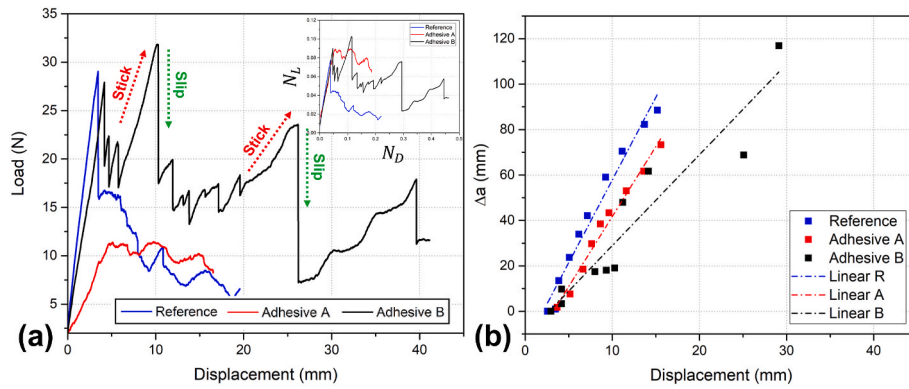
Fig. 7. Representative response of the CFRP DCB specimens: a) load-displacement curves "top right corner for the normalized N_L vs. N_D curves" and b) Crack length propagation as a function of the crosshead displacement.

displacement. Due to this stick-slip nature, the crack propagation speed for the modified adhesive B (15.63 ± 0.87 mm/mm) is found to be approximately half of its reference counterpart (27.32 ± 0.89 mm/mm).

In the case of CFRP adherends (see Fig. 7a), the same observations regarding the global load-displacement behavior still prevail. Although the maximum/peak load of the reference and adhesive B are similar in this case, the stick-slip feature is clear in the case of adhesive B. This directly suggests that the crack propagation should be able to capture this phenomenon in the form of sudden propagations in the crack length (see Fig. 7b). A direct correlation, between the load-displacement curve (Fig. 7a) for adhesive B and the jumps in its corresponding crack growth (Fig. 7b), can be made. For instance, the first highlighted stick-slip location on Fig. 9a occurs at approximately a displacement of 10 mm. This crack length at this specific displacement demonstrates a sudden propagation from approximately 20 to 40 mm. The same feature is captured again at the displacement of ~25 mm, stick-slip feature (Fig. 7a) corresponding to a crack length change (Fig. 9b) from approximately 70 to 120 mm. Unlike adhesive B, both the reference and adhesive A demonstrate a fast crack growth and a typical softening region beyond the peak load. Besides, the crack growth rate for the CFRP adherends (Fig. 7b) confirms the same Al adherends observation with the reference having the fastest rate (7.29 ± 0.44 mm/mm), followed by adhesive A (6.16 ± 0.32 mm/mm) and the slowest rate for adhesive B (4.00 ± 0.47 mm/mm). The slower crack growth rate is a result of the crack propagating inside the adhesive layer in comparison to the fast crack growth at the interface. From a practical point of view, in order to

have more time to react to the crack upon detection, the interfacial failure of bonded structures is not preferable.

To better understand the macroscopic response of the DCB specimens, the aforementioned findings should be complemented with the fractography analysis. According to Blackman [44], such initiation "slip" and arrest "stick" points and their associated crack lengths can be identified on the fractured surfaces. Moreover, a direct correlation between these points and the energy release rate R-curve can be made as discussed later in section 5.3. Thus, Fig. 8 summarizes the 3D height map of the fractured surfaces for both Al and CFRP adherends as well as the three adhesive types (reference, adhesive A and adhesive B). In case of Al adherends (Fig. 8a–c), only the reference adhesive demonstrates a pure adhesive failure (Fig. 8a) while adhesive A failure is mostly adhesive with minor cohesive failure (Fig. 8b) and a mixture of adhesive-cohesive failure in the case of adhesive B (Fig. 8c). This is in a good agreement with the macroscopic observations from the load-displacement point of view and the stick-slip feature in the case of adhesive B. The fractured surfaces are a bit different in the case of the CFRP adherends (Fig. 8d–f). For the reference and adhesive A cases (Fig. 8d and e), a perfect adhesive failure prevails. However for adhesive B (see Fig. 8f), again a mixture of adhesive-cohesive failure is dominant.

5.3. DCB Mode I energy release rate (G_I)

Based on the five repeats, tested for each adherend and each adhesive type, the initiation G_I values are summarized in Fig. 9. The calculations
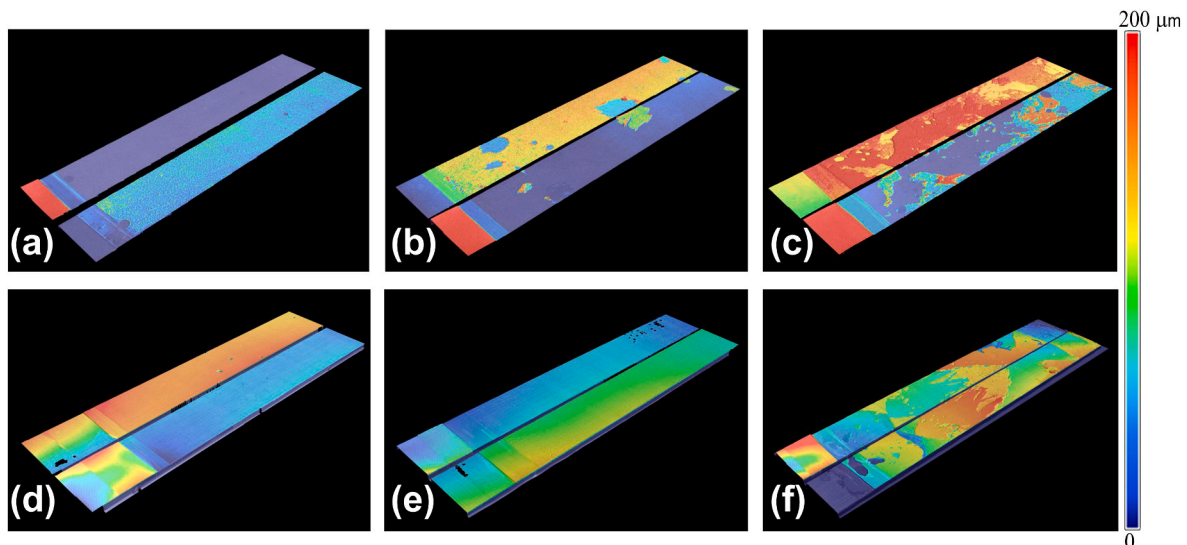

Fig. 8. 3D visualization of the height map of the fractured surfaces of: a) Al-REF, b) Al-A, c) Al-B, d) CFRP-REF, e) CFRP-A and f) CFRP-B.
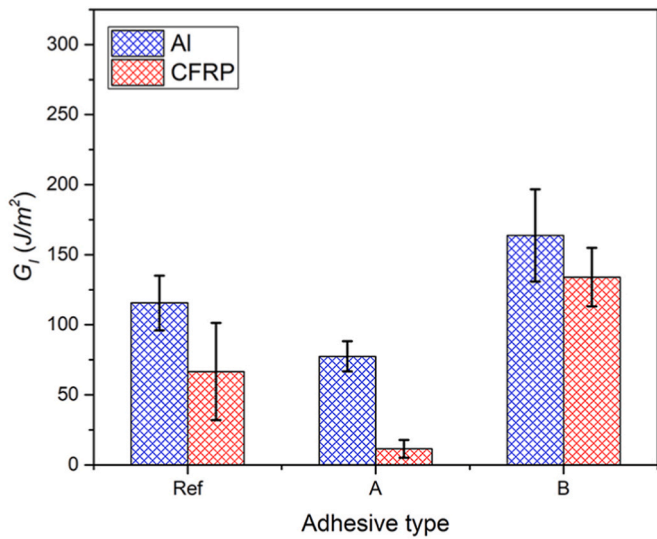
Fig. 9. DCB Mode I energy release rate (G_I) for the three adhesive types on both Al and CFRP adherends.

of the initiation G_I is based on the data reduction techniques detailed in section 4. The general trend, in all cases, is the same with adhesive B significantly improving the initiation G_I regardless of the adherend's material, and adhesive A adversely affecting it compared to the reference case. For the Al adherends, the G_I of adhesive B is 43% higher than the G_I of the reference adhesive; while G_I of adhesive A is 33% lower than the reference adhesive counterpart. In the case of the CFRP adherend, it is found that G_I for adhesive B is 100% higher than the G_I of the reference adhesive; while G_I of adhesive A is 78% lower than the reference adhesive counterpart. This can be attributed to the improvement of both adhesion and cohesion by the introduction of phosphate derivate of TA, in the case of adhesive B, which increased the amount of hydrogen bonding to CFRP material, and more effective crosslinking during adhesive curing. Lower values for adhesive A, compared to the reference counterpart, are a reflection of a weak structure, and thus this requires further investigation of the crack propagation nature and the accompanying failure mechanisms.

The correlation between the R-curve and the fractured surfaces is depicted in Fig. 10 for Al and CFRP adherends, bonded with the three adhesive types. The calculation of the propagation G_I is based on the detailed assumptions, previously discussed in section 4. For the sake of the direct correlation, the 2D optical images of the fractured surfaces are overlaid, to scale, on top of the R-curves with the tip of the Teflon insert
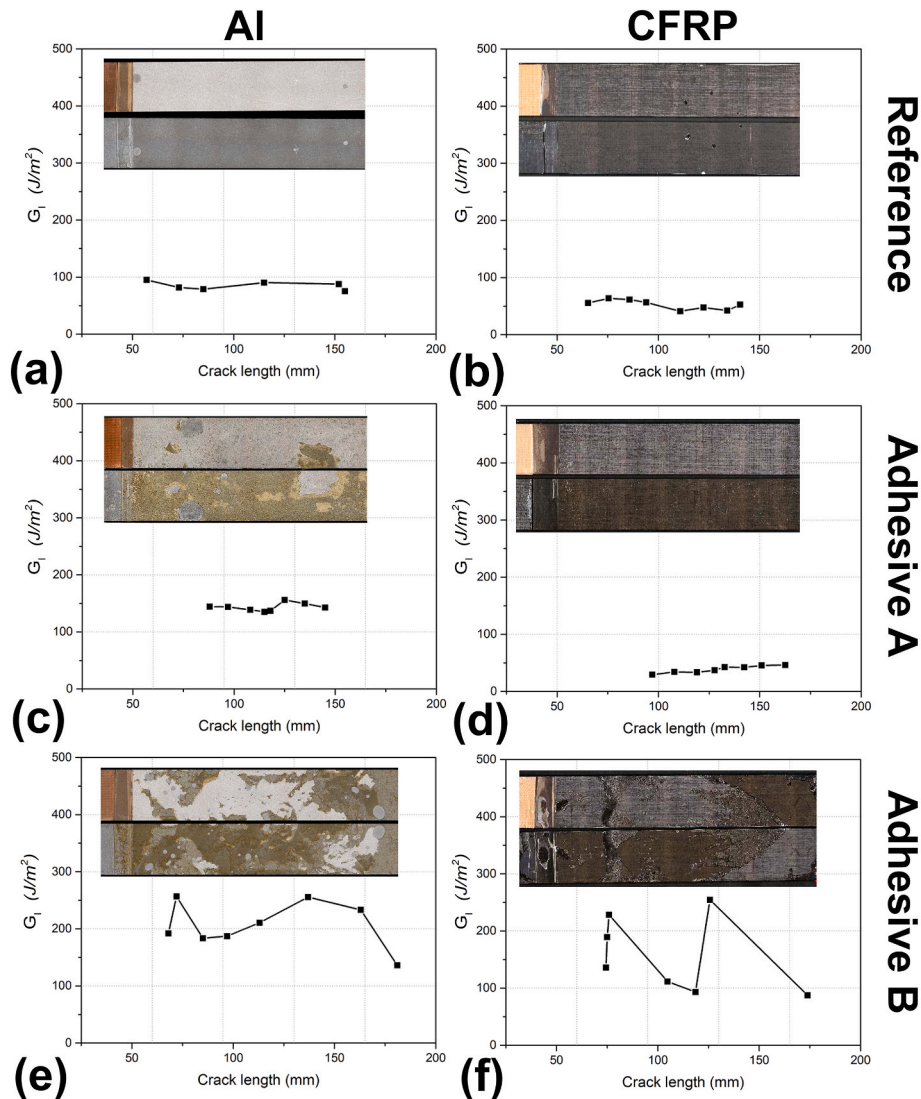

Fig. 10. R-curve along with the fractured surfaces of: a) Al-REF, b) CFRP-REF, c) Al-A, d) CFRP-A, e) Al-B and f) CFRP-B.

coinciding with the initial crack length (~50 mm). For the reference adhesive (Fig. 10a and b) regardless of the adherend type, the G_I value, as a function of the crack length, is almost stable and relatively low, which correlates well with the failure nature being an adhesive failure. For the adhesive A case (Fig. 10c and d), again the trend for G_I is almost constant, indicating an adhesive failure, except for the transition locations from one interface to the other in the Al case, which is directly reflected as a slight increase in the G_I value. For the CFRP case, such transition is not observed, and thus G_I does not show a significant change. Only in the case of adhesive B (Fig. 10e and f) the G_I trend is completely different. For both Al and CFRP, the G_I demonstrates a higher and fluctuating trend which is more significant in the CFRP case. This again coincides very accurately with the crack locus shift locations from cohesive "stick" to adhesive "slip" failure and vice-versa as reported by Heide-Jørgensen et al. [45].

In order to develop a better understanding of the fracture nature, Fig. 11 depicts representative specimens for each adhesive type on the Al substrate along with a schematic interpretation of the crack propagation path. This is chosen to solely explain and analyze the phenomena while the same argument applies for the CFRP adherends. In the case of the reference adhesive (Fig. 11 a and b), an adhesive failure (AF) is observed leaving one adherend with a clean surface while the other adherend is completely covered with the adhesive. The crack propagates only along the interface in this case confirming the poor adhesion between the Al adherend and the reference adhesive as shown schematically in Fig. 11b. In the case of adhesive A, the failure nature is a bit different. As previously highlighted by the height maps (Fig. 8b), the dominant failure is again AF with regions of transition from one interface to another. Another interesting phenomenon observed for adhesive A is the presence of what is referred to her as the peel effect, Fig. 10d. Weak adhesive forces between adhesive A and the adherends caused its peeling from both adherends simultaneously. In addition, cohesive failure (CF) is observed in the form of orphan dots in the sense that they are "isolated/not-connected" adhesive traces remaining on the surfaces of both adherends (see Fig. 11c). For the adhesive B case, the fractured surfaces are completely different. It is very clear that a mixture of AF and CF occurred (Fig. 11e). It is even more interesting to observe the transition

from one failure mechanism to the other, i.e. AF to CF and then back to AF. Moreover, this transition especially from CF to AF can alternate between the two adherend surfaces as schematically shown in Fig. 11f. This confirms the observed macroscopic load-displacement response including the stick-slip phenomenon.

Nevertheless, an in-depth analysis of the chemical structure can further enrich the discussion and shed lights on the reasons for the observed phenomena. Thus, Fig. 12 presents a schematic representation of the intermolecular interactions within the adhesive and the influence of the modified TA on the cohesive and adhesive strengths. Dual epoxy functionality of DGEBA molecule enables dense packing of 3D polymer network of the reference adhesive (see Fig. 12a). The aromatic cores of BPA provide stability and chemical resistance of such system, but also high rigidity and brittle nature. During the reaction of epoxy groups of DGEBA and isophorone diamine (cross-linker), the hydroxyl groups are formed which enable better adhesion. Thus, DGEBA is most commonly used in epoxy adhesive formulation.

When introducing bio-based products such as TA, several benefits are expected. TA consists of ten phenolic cores that are significantly improving its thermal stability and fire-resistance [46]. Those phenolic cores are connected via ester linkages giving flexibility to the molecule. Numerous hydroxyl groups are capable of improving both the cohesion and adhesion properties due to the intermolecular hydroxyl bonding. Functionalized TA with EPH has ten epoxy groups as determined by EEW, one per each phenolic core (component A). Fig. 12 b shows that this bulky molecule doesn't allow as dense packing as the reference does (Fig. 12 a). Besides, it can be expected that the multi-functionality of component A is not fully utilized due to the steric hindrance effect. As a result, the cohesive strength is significantly disturbed compared to the reference adhesive case. On the other hand, the adhesive strength is improved due to the hydroxyl bonding between the TA phenolic groups and adherend, which has been recently proven by the bell-peel test [29]. The difference in the chemical structure between component A and B significantly affects the adhesive performance. Fig. 12 c shows the modified TA with 'longer arms' which represent the dual epoxy functionality as an anchor, extended by a phosphoryl group. This design of TA chemical structure drastically improves its reactivity, and those
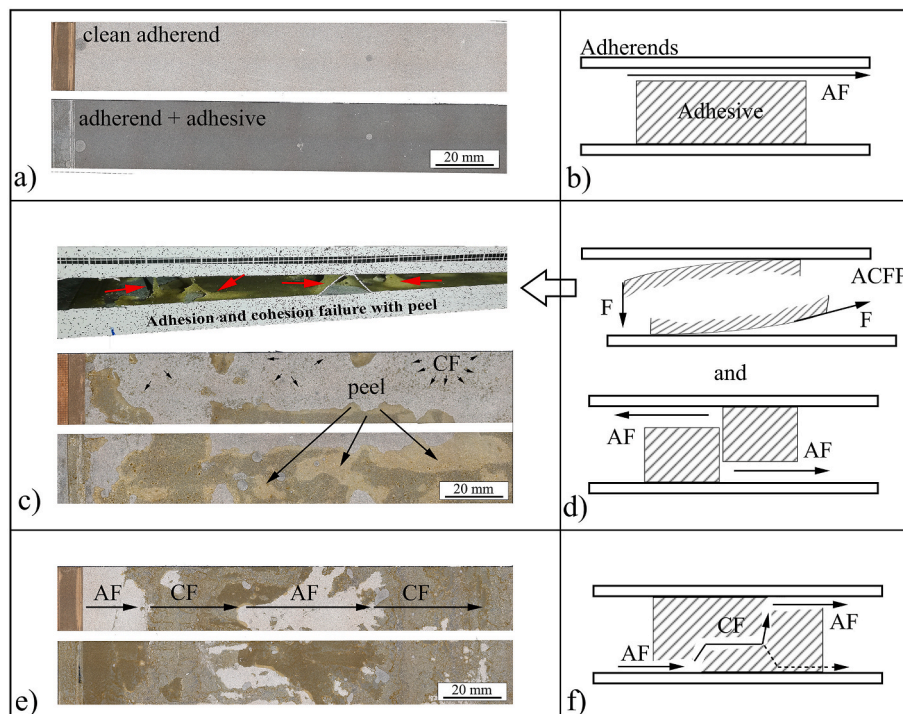

Fig. 11. Fracture analysis and schematic representation of: a and b) Al-REF, c and d) Al-A and e and f) Al-B.
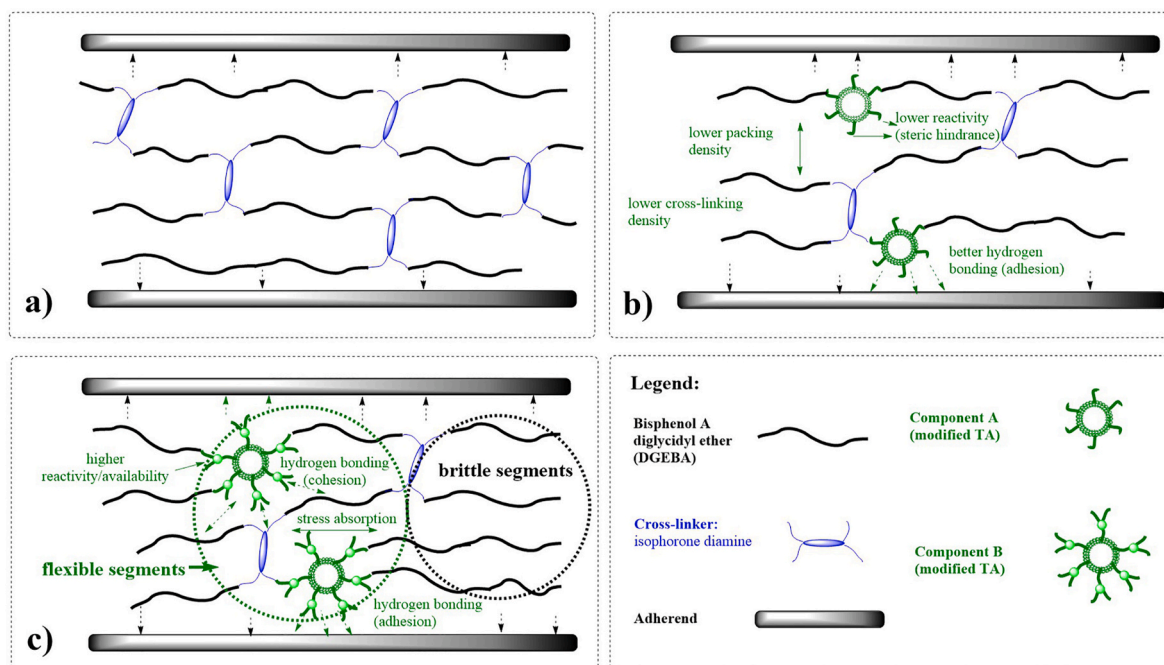
Fig. 12. A schematic representation of the molecular interactions within the adhesive and their influence on adhesive and cohesive strength: a) reference, b) adhesive A and c) adhesive B.

molecules act as hubs in the epoxy polymer network. These hubs of the modified TA (component B) represent the spots that can establish effective stress resistance and energy absorption thanks to the flexibility of TA core. In a system of 15 wt% of component B and 85 wt% of DGEBA, the presence of these segments can affect the fracture mechanisms, i.e. the flexible segments can act as crack arrestors, forcing the crack to further propagate through the brittle segment of the DGEBA, following the principle of minimum potential energy. In addition to the adhesion forces, the flexible segment of component B (shown in Fig. 12c) establishes an improved adhesion when compared to component A, due to better formation of hydroxyl bonding thanks to the phosphoryl group [29,47]. In the example presented in Fig. 12c, when it comes to the flexible segment, the crack has a higher tendency to propagate through the middle of the segment, causing a cohesive failure. When reaching the brittle segment, a dense packing of DGEBA network will cause the change of the crack direction to the adherend interface. The reactivity, better adhesion and the presence of hubs in adhesive B, result in the increase of fracture toughness and the larger areas of cohesive failure compared to adhesive A. The lower amount of cohesive failure of adhesive A, but still higher than reference, suggests the presence of the orphan spots of the weak interconnected component A remaining on the adherend (Fig. 11c) due to the low cohesive strength. In summary, the introduction of epoxy groups to TA via phosphoryl linkage (component B) can significantly contribute to its higher reactivity, and thus better adhesion and cohesion as opposed to the reference commercial DGEBA.

6. Conclusions

In this study, two eco-epoxide components based on TA were synthesized: (A) epoxy functionalized and (B) epoxy ester phosphate derivate of TA and used as a replacement of the BPA based component for bonding Al and CFRP adherends. The effect of these modifications was evaluated by carrying out DCB mode I fracture toughness testing. A robust new technique for in-situ crack monitoring using DIC, based on full field displacement map, was successfully proposed. Experimental findings demonstrated that adhesive A adversely affected the mode I fracture toughness for both Al (−33%) and CFRP (−78%) adherends as

opposed to the reference case. The fracture nature for both the reference and adhesive A was adhesive failure with only an exception in the case of Al being mostly adhesive. On the contrary, compared to the reference adhesive, the implemented modification of adhesive B led to, not only an enhancement in the mode I fracture toughness (∼43% for Al and ∼100% for CFRP), but also a drastic change in the crack propagation path and consequently the nature of the fractured surfaces. In both cases, Al and CFRP, the fractured surfaces supported the macroscopic response in the sense that a mixed cohesive-adhesive failure was observed for adhesive B specimens as opposed to only adhesive failure for the reference adhesive. In addition, the load-displacement curves confirmed the change in the crack propagation path (inside the adhesive vs. at the interface) in the form of stick-slip patterns, regardless of the adherend material type. Such phenomena were also interpreted in the light of the chemical structure of the three adhesive types. The obtained results in this study clearly showed the potential of using eco-epoxy adhesives to improve the adhesion properties and fracture toughness of commercial epoxy systems.

Authors contribution

Mohamed Nasr Saleh: Conceptualization, Methodology, Formal analysis, Writing- Original draft preparation, **Nataša Z. Tomić:** Conceptualization, Investigation, Writing- Reviewing and Editing, **Aleksandar Marinković:** Supervision, **Sofia Teixeira de Freitas:** Validation, Supervision, Writing- Reviewing and Editing.

Data availability

The raw/processed data required to reproduce these findings cannot be shared at this time due to technical or time limitations.

Declaration of competing interest

The authors declare that they have no known competing financial interests or personal relationships that could have appeared to influence the work reported in this paper.

Acknowledgement

References

[1] A.M. Nelson, T.E. Long, A perspective on emerging polymer technologies for bisphenol-A replacement, Polym. Int. 61 (2012) 1485–1491, https://doi.org/10.1002/pi.4323.

[2] E.S. Stevens, Green Plastics: an Introduction to the New Science of Biodegradable Plastics, Princeton University Press, New Jersey, United States, 2001.

[3] J.J. Bozell (Ed.), Chemicals and Materials from Renewable Resources, American Chemical Society, Washington, DC, 2001, https://doi.org/10.1021/bk-2001-0784.

[4] H. Okada, T. Tokunaga, X. Liu, S. Takayanagi, A. Matsushima, Y. Shimohigashi, Direct evidence revealing structural elements essential for the high binding ability of bisphenol A to human estrogen-related Receptor-γ, Environ. Health Perspect. 116 (2008) 32–38, https://doi.org/10.1289/ehp.10587.

[5] https://www.ncsl.org/research/environment-and-natural-resources/policy-update-on-state-restrictions-on-bisphenol-a.aspx#ca, (n.d.).

[6] A.L. Blankenship, K. Coady, Bisphenol A, in: Encycl. Toxicol., Elsevier, 2005, pp. 314–317, https://doi.org/10.1016/B0-12-369400-0/00139-3.

[7] M. Alam, D. Akram, E. Sharmin, F. Zafar, S. Ahmad, Vegetable oil based eco-friendly coating materials: a review article, Arab. J. Chem. 7 (2014) 469–479, https://doi.org/10.1016/j.arabjc.2013.12.023.

[8] C. Asada, S. Basnet, M. Otsuka, C. Sasaki, Y. Nakamura, Epoxy resin synthesis using low molecular weight lignin separated from various lignocellulosic materials, Int. J. Biol. Macromol. 74 (2015) 413–419, https://doi.org/10.1016/j.ijbiomac.2014.12.039.

[9] P.M. Tahir, J.A. Halip, S. Hua Lee, Tannin-based bioresin as adhesives, in: Lignocellul. Futur. Bioeconomy, Elsevier, 2019, pp. 109–133, https://doi.org/10.1016/B978-0-12-816354-2.00007-4.

[10] P. Niedermann, G. Szebenyi, A. Toldy, Novel high glass temperature sugar-based epoxy resins: characterization and comparison to mineral oil-based aliphatic and aromatic resins, Express Polym. Lett. 9 (2015) 85–94, https://doi.org/10.3144/expresspolymlett.2015.10.

[11] F. Jaillet, E. Darroman, A. Ratsimihety, R. Auvergne, B. Boutevin, S. Caillol, New biobased epoxy materials from cardanol, Eur. J. Lipid Sci. Technol. 116 (2014) 63–73, https://doi.org/10.1002/ejlt.201300193.

[12] J. Łukaszczyk, B. Janicki, M. Kaczmarek, Synthesis and properties of isosorbide based epoxy resin, Eur. Polym. J. 47 (2011) 1601–1606, https://doi.org/10.1016/j.eurpolymj.2011.05.009.

[13] S. Ma, X. Liu, Y. Jiang, L. Fan, J. Feng, J. Zhu, Synthesis and properties of phosphorus-containing bio-based epoxy resin from itaconic acid, Sci. China Chem. 57 (2014) 379–388, https://doi.org/10.1007/s11426-013-5025-3.

[14] R. V Gadhave, S. Srivastava, P.A. Mahanwar, P.T. Gadekar, Lignin: renewable raw material for adhesive, Open J. Polym. Chem. 9 (2019) 27–38, https://doi.org/10.4236/ojpchem.2019.92003.

[15] N.E. El Mansouri, Q. Yuan, F. Huang, Characterization of alkaline lignins for use in phenol-formaldehyde and epoxy resins, Bioresources 6 (2011) 2647–2662.

[16] W. Zhang, Y. Ma, C. Wang, S. Li, M. Zhang, F. Chu, Preparation and properties of lignin–phenol–formaldehyde resins based on different biorefinery residues of agricultural biomass, Ind. Crop. Prod. 43 (2013) 326–333, https://doi.org/10.1016/j.indcrop.2012.07.037.

[17] S. Zhao, M.M. Abu-Omar, Biobased epoxy nanocomposites derived from lignin-based monomers, Biomacromolecules 16 (2015) 2025–2031, https://doi.org/10.1021/acs.biomac.5b00670.

[18] S. Zhao, M.M. Abu-Omar, Renewable epoxy networks derived from lignin-based monomers: effect of cross-linking density, ACS Sustain. Chem. Eng. 4 (2016) 6082–6089, https://doi.org/10.1021/acssuschemeng.6b01446.

[19] Q. Yin, W. Yang, C. Sun, M. Di, Preparation and properties of lignin-epoxy resin composite, BioResources 7 (2012), https://doi.org/10.15376/biores.7.4.5737-5748.

[20] C.A. Finch, Advanced wood adhesives technology. A. Pizzi. Marcel dekker, New York, Basel, 1994, Polym. Int. 39 (1996) 78, https://doi.org/10.1002/pi.1996.210390117.

[21] S. Benyahya, C. Aouf, S. Caillol, B. Boutevin, J.P. Pascault, H. Fulcrand, Functionalized green tea tannins as phenolic prepolymers for bio-based epoxy resins, Ind. Crop. Prod. 53 (2014) 296–307, https://doi.org/10.1016/j.indcrop.2013.12.045.

[22] J. Zhang, X. Xi, J. Liang, A. Pizzi, G. Du, S. Deng, Tannin-based adhesive cross-linked by furfuryl alcohol-glyoxal and epoxy resins, Int. J. Adhesion Adhes. 94 (2019) 47–52, https://doi.org/10.1016/j.ijadhadh.2019.04.012.

[23] Y. Shirmohammadli, D. Efhamisisi, A. Pizzi, Tannins as a sustainable raw material for green chemistry: a review, Ind. Crop. Prod. 126 (2018) 316–332, https://doi.org/10.1016/j.indcrop.2018.10.034.

[24] S. Jahanshahi, A. Pizzi, A. Abdulkhani, A. Shakeri, Analysis and testing of bisphenol A—free bio-based tannin epoxy-acrylic adhesives, Polymers 8 (2016) 143, https://doi.org/10.3390/polym8040143.

[25] R. Auvergne, S. Caillol, G. David, B. Boutevin, J.-P. Pascault, Biobased thermosetting epoxy: present and future, Chem. Rev. 114 (2014) 1082–1115, https://doi.org/10.1021/cr3001274.

[26] N. Esmaeili, M. Vafayan, A. Salimi, M.J. Zohuriaan-Mehr, Kinetics of curing and thermo-degradation, antioxidizing activity, and cell viability of a tannic acid based epoxy resin: from natural waste to value-added biomaterial, Thermochim. Acta 655 (2017) 21–33, https://doi.org/10.1016/j.tca.2017.06.005.

[27] X. Fei, F. Zhao, W. Wei, J. Luo, M. Chen, X. Liu, Tannic acid as a bio-based modifier of epoxy/anhydride thermosets, Polymers 8 (2016) 314, https://doi.org/10.3390/polym8090314.

[28] M.C. Basso, A. Pizzi, J. Polesel Maris, L. Delmotte, B. Colin, Y. Rogaume, MALDI-TOF, 13C NMR and FTIR analysis of the cross-linking reaction of condensed tannins by triethyl phosphate, Ind. Crop. Prod. 95 (2017) 621–631, https://doi.org/10.1016/j.indcrop.2016.11.031.

[29] N.Z. Tomić, M.N. Saleh, S.T. de Freitas, A. Živković, M. Vuksanović, J.A. Poulis, A. Marinković, Enhanced interface adhesion by novel eco-epoxy adhesives based on the modified tannic acid on Al and CFRP adherends, Polymers 12 (2020) 1541, https://doi.org/10.3390/polym12071541.

[30] A. Zotti, S. Zuppolini, M. Zarrelli, A. Borriello, Fracture toughening mechanisms in epoxy adhesives, in: A. Rudawska (Ed.), Adhesives, IntechOpen, Rijeka, 2016, https://doi.org/10.5772/65250.

[31] E.H. Saidane, D. Scida, M.J. Pac, R. Ayad, Mode-I interlaminar fracture toughness of flax, glass and hybrid flax-glass fibre woven composites: failure mechanism evaluation using acoustic emission analysis, Polym. Test. 75 (2019) 246–253, https://doi.org/10.1016/j.polymertesting.2019.02.022.

[32] M.Y. Fard, B. Raji, J. Woodward, A. Chattopadhyay, Characterization of interlaminar fracture modes I, II, and I-II of carbon/epoxy composites including in-service related bonding quality conditions, Polym. Test. 77 (2019) 105894, https://doi.org/10.1016/j.polymertesting.2019.05.010.

[33] J. Manterola, J. Zurbitu, J. Renart, A. Turon, I. Urresti, Durability study of flexible bonded joints: the effect of sustained loads in mode I fracture tests, Polym. Test. 88 (2020) 106570, https://doi.org/10.1016/j.polymertesting.2020.106570.

[34] Y.-O. Kim, J. Cho, H. Yeo, B.W. Lee, B.J. Moon, Y.-M. Ha, Y.R. Jo, Y.C. Jung, Flame retardant epoxy derived from tannic acid as biobased hardener, ACS Sustain. Chem. Eng. 7 (2019) 3858–3865, https://doi.org/10.1021/acssuschemeng.8b04851.

[35] J.A. Poulis, J.C. Cool, E.H.P. Logtenberg, UV/ozone cleaning, a convenient alternative for high quality bonding preparation, Int. J. Adhesion Adhes. 13 (1993) 89–96, https://doi.org/10.1016/0143-7496(93)90019-6.

[36] ISO 25217: Adhesives — Determination of the Mode 1 Adhesive Fracture Energy of Structural Adhesive Joints Using Double Cantilever Beam and Tapered Double Cantilever Beam Specimens, 2006, 2009, p. 13.

[37] M. Saeedifar, M.N. Saleh, S.T. De Freitas, D. Zarouchas, Damage characterization of adhesively-bonded Bi-material joints using acoustic emission, Compos. B Eng. 176 (2019), https://doi.org/10.1016/j.compositesb.2019.107356.

[38] M.N. Saleh, M. Saeedifar, D. Zarouchas, S.T. De Freitas, Stress analysis of double-lap bi-material joints bonded with thick adhesive, Int. J. Adhesion Adhes. (2019) 102480, https://doi.org/10.1016/J.IJADHADH.2019.102480.

[39] A. Khudiakova, V. Grasser, C. Blumenthal, M. Wolfahrt, G. Pinter, Automated monitoring of the crack propagation in mode I testing of thermoplastic composites by means of digital image correlation, Polym. Test. 82 (2020) 106304, https://doi.org/10.1016/j.polymertesting.2019.106304.

[40] B.R. Murray, S. Fonteyn, D. Carrella-Payan, K.-A. Kalteremidou, A. Cernescu, D. Van Hemelrijck, L. Pyl, Crack Tip Monitoring of Mode I and Mode II Delamination in CF/Epoxies under Static and Dynamic Loading Conditions Using Digital Image Correlation †, 2018, p. 5225, https://doi.org/10.3390/icem18-05225.

[41] ASTM D5528-01, Standard test method for mode I interlaminar fracture toughness of unidirectional fiber-reinforced polymer matrix composites, Am. Stand. Test. Methods. 3 (2014) 1–12, https://doi.org/10.1520/D5528-13.2.

[42] S. Heide-Jørgensen, M.K. Budzik, Crack growth along heterogeneous interface during the DCB experiment, Int. J. Solid Struct. 120 (2017) 278–291, https://doi.org/10.1016/j.ijsolstr.2017.05.013.

[43] R. Lopes Fernandes, S. Teixeira de Freitas, M.K. Budzik, J.A. Poulis, R. Benedictus, From thin to extra-thick adhesive layer thicknesses: fracture of bonded joints under mode I loading conditions, Eng. Fract. Mech. 218 (2019) 106607, https://doi.org/10.1016/j.engfracmech.2019.106607.

[44] B.R.K. Blackman, Handbook of adhesion technology, Handb. Adhes. Technol. (2011), https://doi.org/10.1007/978-3-642-01169-6.

[45] S. Heide-Jørgensen, S. Teixeira de Freitas, M.K. Budzik, On the fracture behaviour of CFRP bonded joints under mode I loading: effect of supporting carrier and interface contamination, Compos. Sci. Technol. 160 (2018) 97–110, https://doi.org/10.1016/j.compscitech.2018.03.024.

[46] Y.-O. Kim, J. Cho, Y.N. Kim, K.W. Kim, B.W. Lee, J.W. Kim, M. Kim, Y.C. Jung, Recyclable, flame-retardant and smoke-suppressing tannic acid-based carbon-fiber-reinforced plastic, Compos. B Eng. 197 (2020) 108173, https://doi.org/10.1016/j.compositesb.2020.108173.

[47] J.C. Summerton, G.M. Martin, J.D. Evanseck, M.S. Chapman, Common hydrogen bond interactions in diverse phosphoryl transfer active sites, PloS One 9 (2014), e108310, https://doi.org/10.1371/journal.pone.0108310.